Field Testing of Repurposed Electric Vehicle Batteries for Price-Driven Grid Balancing

B. Faessler[1,2,3], P. Kepplinger[1,2], and J. Petrasch[2*]

[1]Josef Ressel Center for Applied Scientific Computing in Energy, Finance, and Logistics, Vorarlberg University of Applied Sciences, Hochschulstrasse 1, 6850, Dornbirn, Austria
[2]Energy Research Center, Vorarlberg University of Applied Sciences, Hochschulstrasse 1, 6850, Dornbirn, Austria
[3]Faculty of Engineering and Science, University of Agder, Jon Lilletuns vei 9, 4879, Grimstad, Norway
**Corresponding author: joerg.petrasch@fhv.at*

ABSTRACT

As electric cars become more widespread, the disposal and recycling of used batteries will become an important challenge. Typically, vehicle batteries are replaced if their capacity drops to 70–80% of initial capacity. However, they may still be useful for stationary applications.
In this paper, results from a field test of a molten salt high-temperature electric vehicle battery repurposed as stationary storage for grid balancing are presented. In a previous study, we have shown that a mixed integer linear programming control strategy driven by a spot-market price for electricity is best suited for an implementation on hardware with limited computational resources.
A 14-day experiment resulted in a round-trip energy efficiency (converter-battery-converter) of about 74.4%. The earnings per battery capacity per day achieved in this period amounted to 7.38 €/MWh. An error analysis of the model underlying the optimization showed a root mean square error of 7.6% between the estimated and measured state of charge.
The field test implementation shows a substantial economic deviation of 37.3% between theoretical and physical potential of grid-balancing measures due to model inaccuracies and technical characteristics, thereby demonstrating the urgent need for field tests of repurposed electric vehicle batteries for stationary applications.

Keywords: Grid Balancing, Distributed Storage, Autonomous Optimization, Repurposed Vehicle ZEBRA Battery, Modeling

NOMENCLATURE

c	Pseudo-cost function (€/MWh)
$E_{\mathrm{AC,in}}$	Energy imported (Wh)
$E_{\mathrm{AC,out}}$	Energy exported (Wh)
E_{el}	Electrical energy content (J)
E_{loss}	Constant battery energy loss (Wh)
E_{err}	Energy estimation error (Wh)
n	Total number of data points (–)
n_{cycle}	Battery charge cycles (–)
n_{d}	Total amount of seconds per day (s)
P_{AC}	Alternating power (W)
P_{DC}	Direct power (W)
P_{loss}	Constant battery loss (W)
s_{earn}	Achieved earnings (€)
SOC	State of charge (%)
R^2	Coefficient of determination (–)
t	Time (s)
t_{d}	Day-time function (s)
x_{c}	Decision variable: charging (–)
x_{d}	Decision variable: discharging (–)
u_{DC}	Decision variable on DC power side (–)
η_{bat}	Battery efficiency (–)
η_{in}	Charging converter efficiency (–)
η_{out}	Discharging converter efficiency (–)
η_{rt}	Round-trip efficiency (–)
ΔE_{err}	Energy estimation error (kWh)

1 INTRODUCTION

The electrical energy market is currently facing new challenges. Boßmann et al. [1] stated that load curves will substantially change due to evolving electricity demand. Since renewable electricity generation, which is volatile by nature, adversely affects grid operation [2], [3], additional grid-balancing measures such as specific strategies and energy storage facilities will become necessary [4]–[6] in the foreseeable future.

Aggregation of small, distributed loads and storage systems for demand side management (DSM), along with the deployment of control strategies with the specific aim of balancing the grid is considered a promising approach [4], [7], [8]. More specifically, battery storage systems have been proposed for distributed approaches [9], as 1) their time scales will soon range from seconds to days [10], 2) they are practically maintenance-free [11], 3) they are quick to respond [12], and 4) they are highly efficient [13], [14], exhibiting total round-trip efficiencies (converter-battery-converter) ranging from 65% to almost 90% [15].
Several types of battery technologies, using a range of cell chemistries [5], [14], have been investigated for grid-tied balancing approaches [16]–[21].

In order to reduce costs, systems that already include battery storage but do not entirely utilize the available capacity at all times, have been proposed. In this context, electric vehicles (EV) [25]–[30], battery bank systems combined with photovoltaics [22], [23] or wind farms [24] have been discussed. Another option to help offset costs is to use repurposed EV batteries [31], [32]. Generally, EV batteries are exchanged if their capacity falls to 70–80% of their initial capacity [31]; at this point, they still have sufficient capacity for stationary applications. Second use of batteries will also reduce their ecological footprint [33], [34]. The German vehicle manufacturer Daimler has announced [35] plans to reuse old EV batteries in a large stationary storage facility with a capacity of 13 MWh. Reusing EV batteries as distributed stationary storage for grid-balancing measures on the kWh-scale has been discussed in previous publications [33], [36], [37]. However, no physical implementation for grid balancing is known to the authors.

The current paper presents a field test of a stationary retrofitted EV battery for grid balancing. A ZEBRA (Zero Emission Battery Research Activities) battery, decommissioned from a THINK City [38] vehicle, is incorporated into a stationary setup. An in-house controller software autonomously optimizes the operation based on the Austrian day-ahead electricity market as suggested by the authors previously [9]. Therein we investigated autonomous control algorithms featuring different battery model complexities with respect to computational costs and the resulting control optimality. Linear optimization routines were shown to be best suited for a physical implementation on a control system with limited computational resources. The economic performance and battery efficiencies are evaluated using an energy monitoring system. The error in the battery model is evaluated by comparing to the physical behavior of the ZEBRA battery. Moreover, we identify the difference in earnings between the physical implementation and theoretical simulation results.

2 EXPERIMENTAL SETUP

The schematics of the stationary battery storage system is shown in Fig. 1a. It comprises a repurposed EV battery including a battery management system (BMS), an embedded control hardware (ECH), an energy monitoring system, and two AC/DC converters. The EV battery is based on a repurposed high-temperature ZEBRA battery. The cell chemistry relies on the reaction of sodium with nickel chloride [39]. The redox reaction [40] is:

$$2\mathrm{Na} + \mathrm{NiCl_2} \underset{charge}{\overset{discharge}{\rightleftharpoons}} 2\mathrm{NaCl} + \mathrm{Ni} \qquad \text{Eq. 1}$$

The ZEBRA battery used has a capacity of 28.2 kWh by comprising individual battery cells. Detailed battery parameters are listed in Table 1 of the Appendix.
The ECH consists of a BeagleBone Black – Rev C [41] and a serial cape [42] integrating a CAN (Controller Area Network) bus [43] transceiver. The ECH manages the communication via CAN bus and Modbus TCP [44] between the hardware components. Furthermore, the ECH determines the operation mode (charge, discharge, idle) of the battery by optimization, minimizing an objective function calculated from a pseudo-cost function (PCF), while keeping the battery's state of charge (SOC) within given operational bounds. The PCF represents the operator's intention and is fetched from a PCF distribution system through a mobile-network-enabled router via TCP/IP.
For charging and discharging, separate converters are used. For charging, the original EV single-phase charger [45] is used. The DC charge characteristics is shown in Fig. 1b. Charging power is controlled by the BMS via a pulse-width modulation (PWM) signal depending on the battery state. The charging strategy relies on a constant current constant voltage (CCCV) procedure. Up to 80% SOC, constant current is applied followed by charging at a constant voltage. Thereby, the charging current drops automatically with increasing SOC. The three drops in current, voltage, and power are caused by the activation of auxiliary temperature control systems to maintain the internal battery temperature. Discharging at 80% SOC is induced by a battery cell balancing process. The charging converter efficiency ranges from 95% for 3.2 kW to 90% for 0.4 kW [45]. The average DC charging power measured during a charging process is 1.49 kW. Details are given in Table 2 of the Appendix.
Since the charger is not designed for discharging, a three-phase converter from Fronius [46], including a data manager module, is integrated into the stationary setup. The discharging power can be controlled continuously via Modbus TCP from 0 – 100% of the maximum power. The efficiency ranges from about 90% to almost 97.5% depending on the output power [46]. Preliminary measurements showed that the average DC discharging power between 20% and 100% SOC is 8.64 kW, i.e., 5.8 times the DC charging power. Details are given in Table 3 of the Appendix.
All energy flows through the converters are measured and recorded by an energy monitoring system from Algodue [47]. The ECH fetches measured energy data via Modbus TCP. The measured in- and output energy flows also include the powering of the energy counter and the BMS. The energy flows are stored at a resolution of 15 minutes. Details are given in Table 4 of the Appendix.

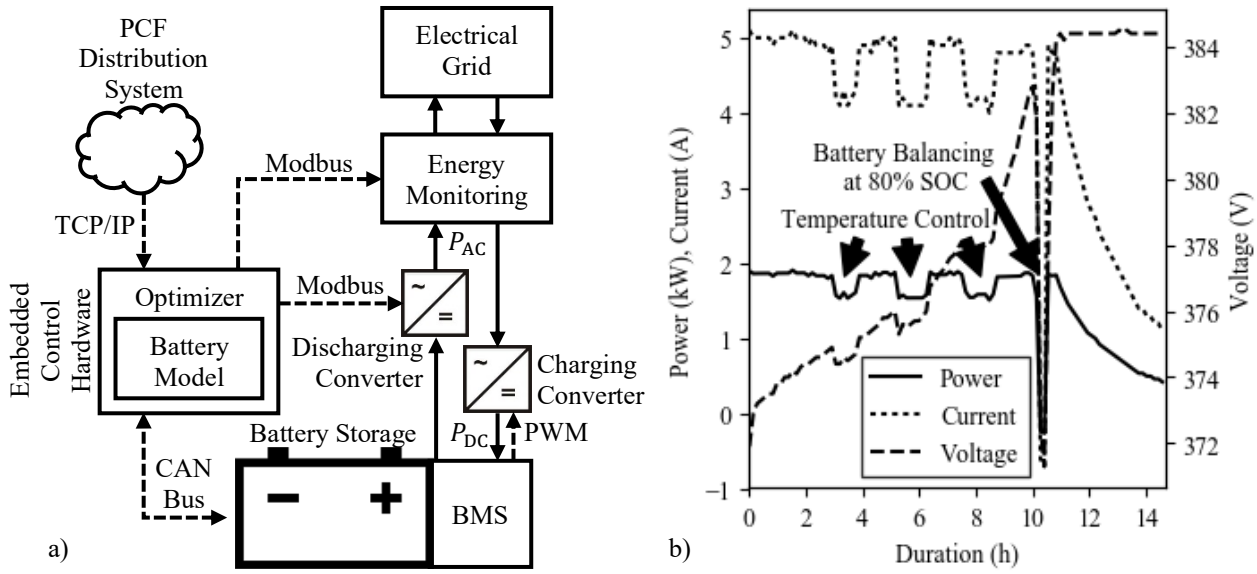

Fig. 1: a) Schematics of the stationary battery storage system including all hardware components. b) DC charge characteristics of a ZEBRA battery storage system.

3 MODELING AND OPTIMIZATION

As shown in [9], a linear battery model predicts the dynamic behavior of the ZEBRA battery with reasonable accuracy. The linear battery model is described as follows,

$$\frac{\mathrm{d}E_{\mathrm{el}}}{\mathrm{d}t} = P_{\mathrm{DC}}(t) - P_{\mathrm{loss}}. \qquad \text{Eq. 2}$$

E_{el} reflects the electrical energy content of the battery, P_{DC} the DC charging/discharging power, and P_{loss} the constant losses. P_{loss} includes internal losses via battery cell resistance and auxiliary heating and cooling power. It is estimated once a day by fitting the model using seven days of historic DC power and SOC data. More specifically, using the integral form of Eq. 2 for a given time window $[t_0, t_n]$,the least squares problem can be formulated as follows,

$$\min_x \|a \cdot x - b\|^2, \text{where} \qquad \text{Eq. 3}$$

$$a_i = i \text{ and} \qquad \text{Eq. 4}$$

$$b_i = \left(E_{\mathrm{el}}(t_0) - E_{\mathrm{el}}(t_i) + \int_{t_0}^{t_i} P_{\mathrm{DC}}(t)\, dt\right), \forall i \in \{1, \cdots, n\}. \qquad \text{Eq. 5}$$

The optimization approaches presented in [9], [48] are adapted to account for different charging and discharging power and converter efficiencies. For a given PCF, $c(t)$, at a resolution of Δt in the time window $[t_0, t_n]$, the optimization problem can be formulated as:

$$\min_{u_{\mathrm{DC}}} \int_{t_0}^{t_n} c(t) \cdot P_{\mathrm{AC}}(u_{\mathrm{DC}}(t))\, dt, \text{s.t.} \qquad \text{Eq. 6}$$

$$E_{\mathrm{el,min}} \leq E_{\mathrm{el}}(t) \leq E_{\mathrm{el,max}},\ t_0 \leq t \leq t_n \qquad \text{Eq. 7}$$

Here, P_{AC} denotes the AC power resulting at the electrical grid, accounting for power conversion. Based on previous work [9], simulations reveal a strong correlation between the earnings and the variance of the PCF. Therefore, the 15-min-based stock market prices for electricity, published by Energy Exchange Austria (EXAA) [49] daily on working days at 12 noon for the next 36 hours, is used. To apply the optimization to the linear battery model, we formulate a mixed integer linear program (MILP) as follows:

$$\min_{u_{\mathrm{DC}}} \sum_{i=1}^{n} c_i(t) \cdot \left(u^{+}_{\mathrm{DC},i} \cdot \eta_{\mathrm{in}}^{-1} \cdot P_{\mathrm{DC,max}} - u^{-}_{\mathrm{DC},i} \cdot \eta_{\mathrm{out}} \cdot P_{\mathrm{DC,max}}\right) \cdot \Delta t, \text{s.t.} \qquad \text{Eq. 8}$$

$$E_{\mathrm{el,min}} \leq E_{\mathrm{el},0} + \sum_{i=1}^{j} \left[u^{+}_{\mathrm{DC},i} \cdot P_{\mathrm{DC,max}} - u^{-}_{\mathrm{DC},i} \cdot P_{\mathrm{DC,max}} - P_{\mathrm{loss}}\right] \cdot \Delta t \leq E_{\mathrm{el,max}}, \forall j \in \{1, \cdots, n\}, \qquad \text{Eq. 9}$$

$$0 \leq x_{c,i} + x_{d,i} \leq 1, x_{c,i}, x_{d,i} \in \{0,1\}\ \forall i, \quad \text{Eq. 10}$$

$$u^{+}_{DC,i} \leq u^{+}_{DC,max} \cdot (1 - x_{d,i}), \quad \text{Eq. 11}$$

$$u^{+}_{DC,i} \geq u^{+}_{DC,min} \cdot x_{c,i}, \quad \text{Eq. 12}$$

$$u^{-}_{DC,i} \leq u^{-}_{DC,max} \cdot (1 - x_{c,i}), \quad \text{Eq. 13}$$

$$u^{-}_{DC,i} \geq u^{-}_{DC,min} \cdot x_{d,i}, \quad \text{Eq. 14}$$

$$u^{+}_{DC,i} \leq u^{+}_{DC,max} \cdot (x_{c,i} + x_{d,i}), \quad \text{Eq. 15}$$

$$u^{-}_{DC,i} \leq u^{-}_{DC,max} \cdot (x_{c,i} + x_{d,i}). \quad \text{Eq. 16}$$

To account for different charging and discharging DC powers, we introduce two continuous decision variables, $u^{+}_{DC,i}$ and $u^{-}_{DC,i}$ for each time step, indicating charging and discharging separately. At the maximum charging DC power, $u^{+}_{DC,max}$ is set to 1; at the maximum discharging DC power, $u^{-}_{DC,max}$ is set to 5.8 reflecting the discharging to charging power ratio (cf. Section 2). The composite decision variable is then given by $\boldsymbol{u}_{DC} = \boldsymbol{u}^{+}_{DC} + \boldsymbol{u}^{-}_{DC}$. Converter efficiencies η_{in}, η_{out} are included linearly in the objective function. The charging efficiency, η_{in}, is set to 90.0%, the discharging efficiency, η_{out}, to 95.0%. Since the converters perform inefficiently up to 20% of their maximum output power, the boundary conditions exclude charging or discharging for lower values, reflecting by Eq. 11 – Eq. 16. Binary variables $x_{c,i}$, $x_{d,i}$ are used to exclude discharging during charging and vice versa. The initial electrical energy content is denoted by $E_{el,0} = E_{el}(t_0)$. A minimum and maximum electrical energy content, $E_{el,min}$ and $E_{el,max}$, respectively, bound the battery operation. The optimization routine is executed every 15 minutes using the SOC measured on the physical device as the initial state of the battery model. Thus, the accumulation of large deviation between measured and modelled SOC over time is avoided.

4 RESULTS

The results obtained show the performance of the storage system during the experiment based on price-driven, on-site optimized operation and reveal the battery model accuracy used in the optimization in comparison to the physical behavior. Experimental results achieved were recorded from 24 May 2017, 4:15 until 6 June 2017, 9:00.

4.1 Battery Performance

Based on the energy monitoring measurements, the round-trip efficiency (converter-battery-converter) η_{rt} is calculated:

$$E_{AC,in}(t_0, t_n) = \int_{t_0}^{t_n} P_{AC,in}(t)\, dt, \quad \text{Eq. 17}$$

$$E_{AC,out}(t_0, t_n) = \int_{t_0}^{t_n} P_{AC,out}(t)\, dt, \quad \text{Eq. 18}$$

$$\eta_{rt} = \frac{E_{el}(t_n) - E_{el}(t_0) + E_{AC,out}(t_0, t_n)}{E_{AC,in}(t_0, t_n)}, \quad \text{Eq. 19}$$

where $E_{AC,in}$ is the monitored input and $E_{AC,out}$ the monitored output energy based on the integral of the alternating input power, $P_{AC,in}$, and output power, $P_{AC,out}$, during the period observed. The battery efficiency, η_{bat}, is calculated as

$$\eta_{bat} = \frac{\eta_{rt}}{\eta_{in} \cdot \eta_{out}}. \quad \text{Eq. 20}$$

A full battery charge cycle is defined as a complete turnover of twice the battery capacity. The number of cycles is hence estimated by the energy transferred in and out, $E_{AC,in}$ and $E_{AC,out}$, respectively:

$$n_{cycle} = \frac{(E_{AC,in}(t_0, t_n) \cdot \eta_{in} + E_{AC,out}(t_0, t_n) \cdot \eta_{out}^{-1}) \cdot \eta_{bat}}{2 \cdot E_{el,max}} \quad \text{Eq. 21}$$

For the 14-day duration of the experiment η_{rt} = 74.4%, η_{bat} = 87.0%, and n_{cycle} = 9.43.

Fig. 2 shows the SOC distribution during the experiment. Between the operational bounds of 20% and 100% SOC of the battery, the median is 65.2% SOC, the first quartile is 45.5%, and the third quartile is 79.8%. The peak at 80% SOC is caused by the cell balancing process, cf. Section 2. The peaks at 20% and 100% SOC are provoked by model inaccuracies e.g. the SOC reset during the charging process.

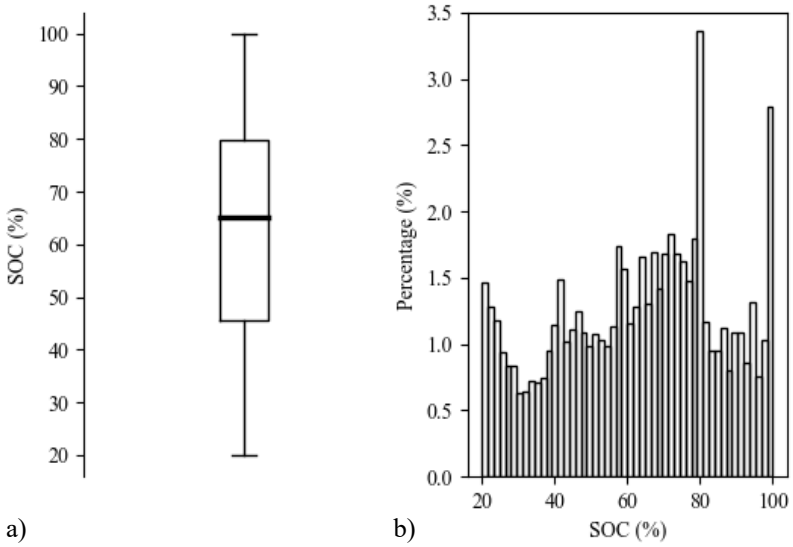

Fig. 2: a) Boxplot and b) histogram of the SOC for the experiment conducted.

Daily estimated battery losses, P_{loss}, and corresponding coefficients of determination, R^2, are calculated, cf. Section 3. Based on P_{loss}, the daily estimated energy losses, E_{loss}, are calculated and shown with the corresponding R^2 in Fig. 3. The estimated losses range from 1.93 W/kWh to 3.54 W/kWh of battery capacity resulting in daily estimated energy losses between 46.32 Wh/kWh and 84.96 Wh/kWh of battery capacity. Assuming the maximum daily energy losses as constant losses during the experiment would lead to a charge energy to loss energy ratio of 10.10%. The R^2 values range from 0.86 to 0.96.

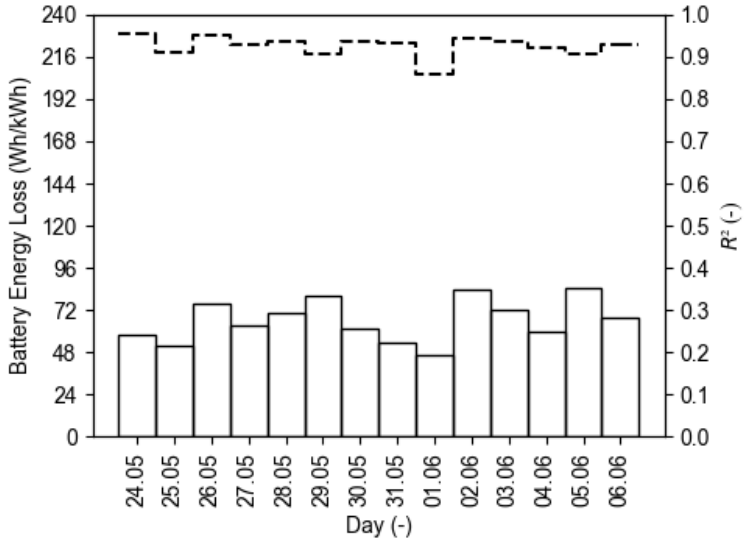

Fig. 3: Daily estimated constant battery losses (solid line) and corresponding R^2 values (dashed line) during the experiment.

4.2 Cost Efficiency Analysis

Fig. 4a shows the box plot of the day-ahead price for the period 24 May 2017, 4:15 until 6 June 2017, 9:00 in total and separated based on the operation mode (charge, discharge, idle). The median of the total day-ahead price observed is 30.20 €/MWh, the first and third quartile are 23.64 €/MWh and 37.54 €/MWh, and the minimum and maximum value are 0.45 €/MWh and 59.00 €/MWh, respectively. For low prices, the predominant state is “charging”, for medium prices, the predominant state is “idle”, and for high prices “discharging” is most common. The histograms in Fig. 4b reveals a strong correlation between price and operation mode.

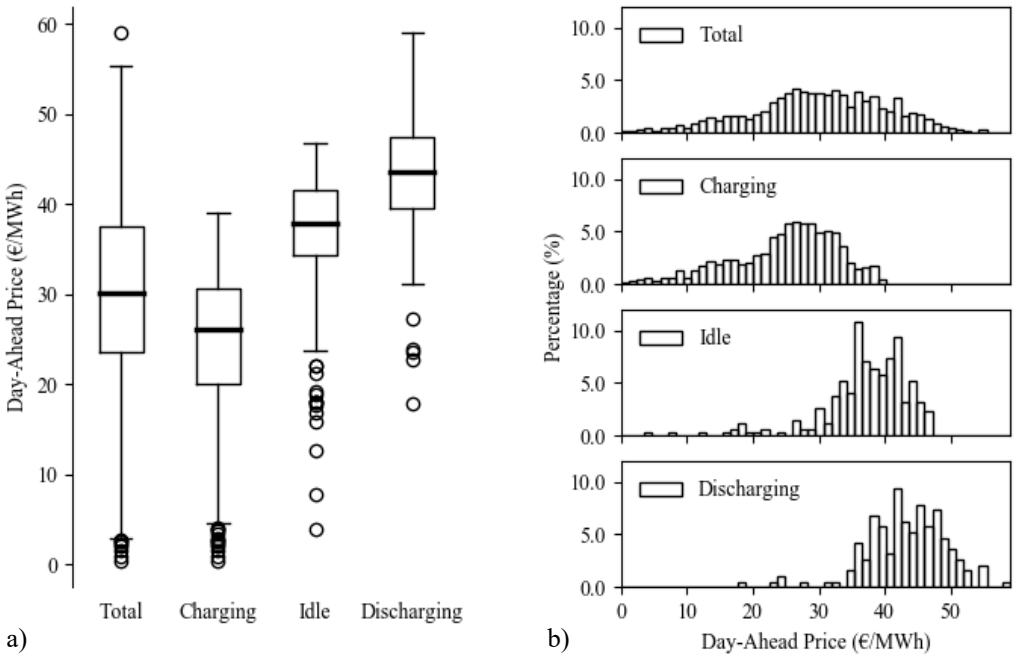

a) b)

Fig. 4: a) Boxplot and b) histogram of the day-ahead stock market price for electricity for the period 24 May 2017, 4:15 until 6 June 2017, 9:00 in total and separated based on the operation mode (charge, discharge, idle).

The earnings achieved per MWh of battery capacity, s_{earn}, during one day are calculated as

$$s_{\text{earn}}(t_0, t_n) = \frac{\int_{t_0}^{t_n} c(t) \cdot \left(E_{\text{AC,in}}(t_0, t_n) - E_{\text{AC,out}}(t_0, t_n)\right)}{E_{\text{el,max}}}, t_0 \leq t \leq t_n. \quad \text{Eq. 22}$$

The potential earnings assuming linear battery behavior are investigated by simulation. To this end, the model is continually initialized at 12 noon, using the corresponding 36 hours day-ahead price and the battery losses estimated during the experiment. The new battery state is calculated and used as initial state for the next day optimization. The resulting potential earnings amount to 11.78 €/MWh of battery capacity per day. In comparison, the earnings realized during the experiment amount to 7.38 €/MWh of battery capacity per day.

4.3 Model Accuracy

To determine the quality of the linear battery model, the estimated SOC is compared to the SOC measured by the BMS. Fig. 5 shows a 36-hour time window, depicting the day-ahead price (PCF), the corresponding decision function, the measured SOC, and the model prediction based on the decision states executed. The case shown represents optimization starting at midnight. It predicts the battery state for 24 hours since the currently available day-ahead price ends at midnight of the following day. Two major instances of model deviations can be observed. The first occurs at approximately 6:15. According to the decision function, the battery should charge. Since the BMS balances the individual battery cells (cf. Section 2), the charging process is interrupted. The second deviation occurs at approximately 14:30. The charging process is interrupted by a battery balancing procedure followed by a short charging period. A sudden change in SOC to 100% occurs at approximately 15:15 since the BMS determines by measuring the cell voltages that the end of charge state is reached.

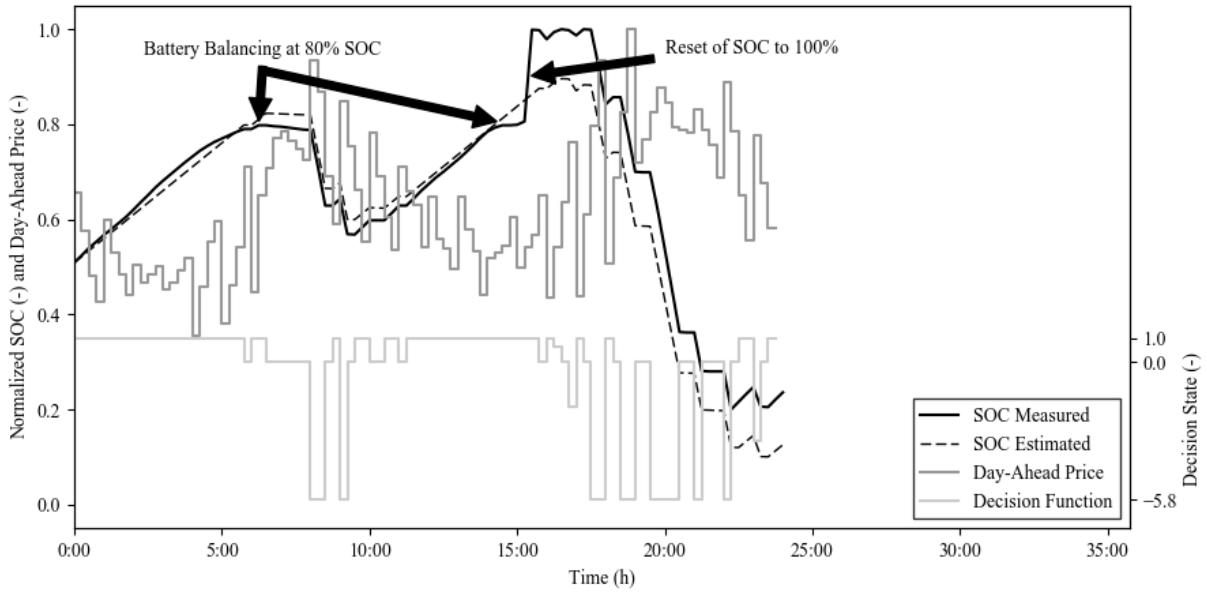

Fig. 5: Exemplary battery operation indicating estimated SOC (dashed black line) and measured SOC (black line) based on the 15 minutes Austrian day-ahead stock market price for electricity (dark grey line). All values on the left axis are normalized with respect to their maximum value. The light grey line indicates the decision states executed on the storage in a 15-minute time interval.

To determine the linear battery model accuracy, the estimated SOC is compared to the SOC measured by the BMS. The root mean square error (RMSE) is calculated between the 24 May 2017, 12:00 and 5 June 2017, 00:00. To this end, every 15 minutes, i.e., Δt = 900 seconds, an estimation of the future SOC (SOC_{est}) for the available day-ahead price time window is calculated and compared to the historic SOC (SOC_{hist}). Introducing the day-time function, $t_{\mathrm{d}}(i)$, which returns the seconds passed for the current date-time since midnight for a given time step i, the calculation of the RMSE reflecting the model error can be formulated as

$$\mathrm{RMSE} = \sqrt{\sum_{j=i}^{i+k}\left(\frac{SOC_{\mathrm{est},j} - SOC_{\mathrm{hist},j}}{k}\right)^2}, i = \{1, \cdots, n\}, \text{where} \qquad \text{Eq. 23}$$

$$k = \begin{cases} \left\lceil \frac{n_{\mathrm{d}} - t_{\mathrm{d}}(i)}{\Delta t} \right\rceil, & 0 \le t_{\mathrm{d}}\,(i) < \frac{n_{\mathrm{d}}}{2} \\ \left\lceil \frac{n_{\mathrm{d}} - t_{\mathrm{d}}(i)}{\Delta t} + \frac{n_{\mathrm{d}}}{\Delta t} \right\rceil & \text{else,} \end{cases} \qquad \text{Eq. 24}$$

where n_{d} is the total number of seconds per day. The resulting RMSE for the experiment yielded to 7.6%. Deviations of the estimated SOC are illustrated in Fig. 6.

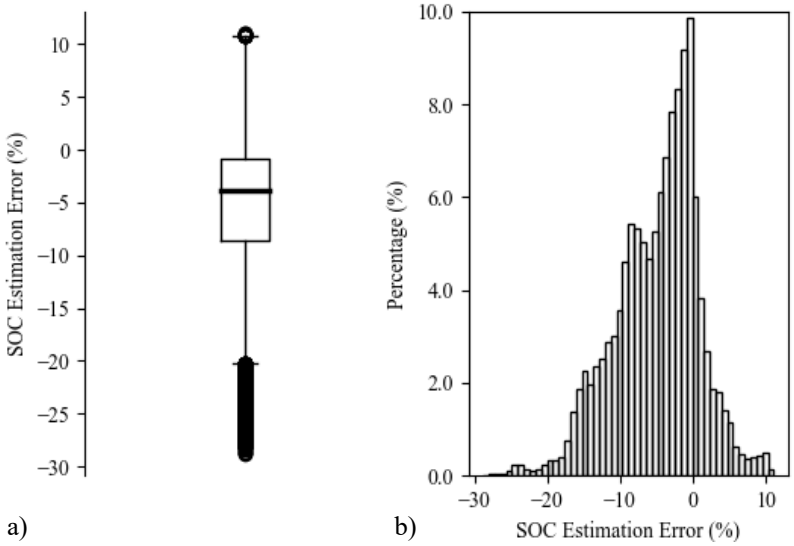

a) b)

Fig. 6: a) Boxplot and b) histogram of the deviation of the estimated to the BMS measured SOC during the experiment.

The deviation between estimated and measured electric energy content of the battery during the experiment is classified according to the mode of operation (charge, discharge, idle), cf. Fig. 7 (left). The energy estimation error is calculated as

$$\Delta E_{\mathrm{err}}^{+} = \int_{T^{+}} P_{\mathrm{DC}}(t)\,dt - \int_{T^{+}} \left(u_{\mathrm{DC}}^{+}(t) \cdot \eta_{\mathrm{in}}^{-1} \cdot P_{\mathrm{DC,max}}\right) dt, \text{ where} \quad \text{Eq. 25}$$

$$T^{+} = \{t_0 \le t \le t_n : u_{\mathrm{DC}}^{+}(t) > 0\}, \text{and} \quad \text{Eq. 26}$$

$$\Delta E_{\mathrm{err}}^{-} = \int_{T^{-}} P_{\mathrm{DC}}(t)\,dt + \int_{T^{-}} \left(u_{\mathrm{DC}}^{-}(t) \cdot \eta_{\mathrm{out}} \cdot P_{\mathrm{DC,max}}\right) dt, \text{ where} \quad \text{Eq. 27}$$

$$T^{-} = \{t_0 \le t \le t_n : u_{\mathrm{DC}}^{-}(t) > 0\}, \text{and} \quad \text{Eq. 28}$$

$$\Delta E_{\mathrm{err}}^{\mathrm{idle}} = \int_{T^{\mathrm{idle}}} P_{\mathrm{DC}}(t)\,dt, \text{ where} \quad \text{Eq. 29}$$

$$T^{\mathrm{idle}} = \{t_0 \le t \le t_n : u_{\mathrm{DC}}^{+}(t) = u_{\mathrm{DC}}^{-}(t) = 0\}. \quad \text{Eq. 30}$$

For charging $\Delta E_{\mathrm{err}}^{+}$ is caused by the assumption of constant charging power (see Section 2). During idling, $\Delta E_{\mathrm{err}}^{\mathrm{idle}}$ is attributed to inaccuracies in modeling the energy required to maintain the internal battery temperature. Deviations $\Delta E_{\mathrm{err}}^{-}$ are largest during discharging due to BMS and converter delay. In Fig. 7b an example of the transition from charging to discharging is shown. The delay is attributed to 1) the time that the BMS needs to perform safety checks and switch from the charge/idle to the discharge mode and 2) the time that the discharge converter needs to execute grid synchronization. 2) consists of a self-test followed by a measurement of frequency, voltage, and phase with subsequent adaptation of output parameters. The median overall delay in the observed period amounted to 88 seconds, where the minimum and maximum delay were 70 seconds and 106 seconds, respectively. Switching from idle to discharge mode shows similar delays. This time lag is not included in the optimization because it introduces nonlinearity in the objective function.

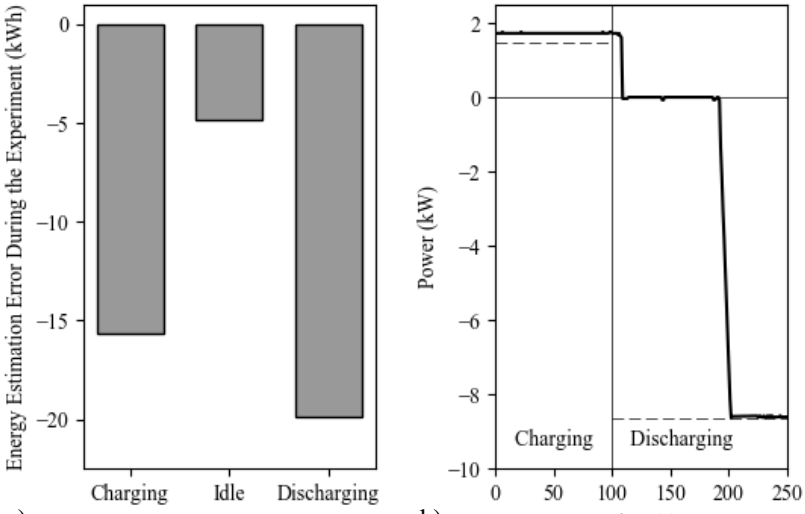

Fig. 7: a) Energy estimation error classified for charging, idle, and discharging during the experiment. b) Exemplary plot of the transition from charging to discharging, showing the deviation between measured (bold line) and estimated DC power (dashed line). For charging, the physically applied DC power is underestimated by the model (upper dashed line). The subsequent discharging process (estimated DC power shown as lower dashed line) shows a delay in switching from charging to discharging

5 CONCLUSION

In this paper, decentralized and on-site optimized grid balancing utilizing a repurposed high-temperature ZEBRA battery storage system is demonstrated experimentally in the field. Based on a previous investigation [9], linear programming routines were used to optimize battery operation based on one-way communicated Austrian quarter-hour day-ahead stock market prices for electricity.

During a 14-day period from 24 May 2017, 4:15 until 6 June 2017, 9:00, the stationary storage system operated with a round-trip efficiency (converter-battery-converter) of 74.4%. In doing so, the system performed 9.43 full battery charge cycles with a median state of charge of 65.2%. An accuracy analysis of the proposed linear battery model shows a root mean square error of 7.6% between the simulated and the measured state of charge during the experiment. In most cases, the state of charge is underestimated due to delayed discharging caused by battery safety check and a grid synchronization process.

Earnings in the observed period amounted to 7.38 €/MWh of battery capacity per day, where the minimum and maximum day-ahead price were 0.45 €/MWh of battery capacity and 59.00 €/MWh of battery capacity, respectively. Although the installation and equipment costs of the presented stationary battery storage cannot be determined, it can be said that the earnings achieved must be significantly higher in order to operate the storage economically. We conclude that the battery must be operated on markets with higher volatility and/or a larger price range to increase the viable earnings.
The potential earnings, found by simulation assuming linear battery behavior, amounted to 11.78 €/MWh of battery capacity per day. The discrepancy of 37.3% to the experimental results can be attributed to insufficiencies in representation of the battery management system, the battery behavior in the model and of the converter characteristics. The significant economic deviations between model and experiment show the urgent need for field tests of grid-balancing strategies to investigate their potential.

ACKNOWLEDGEMENTS

The financial support by the Austrian Federal Ministry of Science, Research and Economy and the National Foundation for Research, Technology and Development is gratefully acknowledged. We gratefully acknowledge financial support for parts of this work, as the stationary battery storage setup, by the FFG Austrian Research Promotion Agency within the framework of the SmartCity Rheintal project (FFG no. 836088).

REFERENCES

[1] T. Boßmann and I. Staffell, “The shape of future electricity demand: Exploring load curves in 2050s Germany and Britain,” *Energy*, vol. 90, pp. 1317–1333, Oct. 2015.
[2] M. Beaudin, H. Zareipour, A. Schellenberglabe, and W. Rosehart, “Energy storage for mitigating the variability of renewable electricity sources: An updated review,” *Energy Sustain. Dev.*, vol. 14, no. 4, pp. 302–314, Dec. 2010.
[3] A. Pina, C. Silva, and P. Ferrão, “The impact of demand side management strategies in the penetration of renewable electricity,” *Energy*, vol. 41, no. 1, pp. 128–137, May 2012.
[4] P. Palensky and D. Dietrich, “Demand Side Management: Demand Response, Intelligent Energy Systems, and Smart Loads,” *IEEE Trans. Ind. Inform.*, vol. 7, no. 3, pp. 381–388, Aug. 2011.
[5] P. J. Hall and E. J. Bain, “Energy-storage technologies and electricity generation,” *Energy Policy*, vol. 36, no. 12, pp. 4352–4355, Dec. 2008.
[6] A. T. Gullberg, D. Ohlhorst, and M. Schreurs, “Towards a low carbon energy future – Renewable energy cooperation between Germany and Norway,” *Renew. Energy*, vol. 68, pp. 216–222, Aug. 2014.
[7] C. A. Hill, M. C. Such, D. Chen, J. Gonzalez, and W. M. Grady, “Battery Energy Storage for Enabling Integration of Distributed Solar Power Generation,” *IEEE Trans. Smart Grid*, vol. 3, no. 2, pp. 850–857, Jun. 2012.
[8] P. Siano, “Demand response and smart grids—A survey,” *Renew. Sustain. Energy Rev.*, vol. 30, pp. 461–478, Feb. 2014.
[9] B. Faessler, P. Kepplinger, and J. Petrasch, “Decentralized price-driven grid balancing via repurposed electric vehicle batteries,” *Energy*, vol. 118, pp. 446–455, Jan. 2017.
[10] K. C. Divya and J. Østergaard, “Battery energy storage technology for power systems—An overview,” *Electr. Power Syst. Res.*, vol. 79, no. 4, pp. 511–520, Apr. 2009.
[11] A. R. Landgrebe and S. W. Donley, “Battery storage in residential applications of energy from photovoltaic sources,” *Appl. Energy*, vol. 15, no. 2, pp. 127–137, Jan. 1983.
[12] P. Mercier, R. Cherkaoui, and A. Oudalov, “Optimizing a Battery Energy Storage System for Frequency Control Application in an Isolated Power System,” *IEEE Trans. Power Syst.*, vol. 24, no. 3, pp. 1469–1477, Aug. 2009.
[13] B. Peng and J. Chen, “Functional materials with high-efficiency energy storage and conversion for batteries and fuel cells,” *Coord. Chem. Rev.*, vol. 253, no. 23–24, pp. 2805–2813, Dec. 2009.
[14] H. Chen, T. N. Cong, W. Yang, C. Tan, Y. Li, and Y. Ding, “Progress in electrical energy storage system: A critical review,” *Prog. Nat. Sci.*, vol. 19, no. 3, pp. 291–312, Mar. 2009.

[15] R. Dufo-López and J. L. Bernal-Agustín, "Techno-economic analysis of grid-connected battery storage," *Energy Convers. Manag.*, vol. 91, pp. 394–404, Feb. 2015.
[16] J. Leadbetter and L. Swan, "Battery storage system for residential electricity peak demand shaving," *Energy Build.*, vol. 55, pp. 685–692, Dec. 2012.
[17] C. Pang, P. Dutta, and M. Kezunovic, "BEVs/PHEVs as Dispersed Energy Storage for V2B Uses in the Smart Grid," *IEEE Trans. Smart Grid*, vol. 3, no. 1, pp. 473–482, Mar. 2012.
[18] M. Bragard, N. Soltau, S. Thomas, and R. W. De Doncker, "The Balance of Renewable Sources and User Demands in Grids: Power Electronics for Modular Battery Energy Storage Systems," *IEEE Trans. Power Electron.*, vol. 25, no. 12, pp. 3049–3056, Dec. 2010.
[19] N. W. Miller, R. S. Zrebiec, R. W. Delmerico, and G. Hunt, "Battery energy storage systems for electric utility, industrial and commercial applications," 1996, pp. 235–240.
[20] H. Qian, J. Zhang, J.-S. Lai, and W. Yu, "A high-efficiency grid-tie battery energy storage system," *IEEE Trans. Power Electron.*, vol. 26, no. 3, pp. 886–896, Mar. 2011.
[21] O. Palizban and K. Kauhaniemi, "Energy storage systems in modern grids—Matrix of technologies and applications," *J. Energy Storage*, vol. 6, pp. 248–259, May 2016.
[22] O. M. Toledo, D. Oliveira Filho, and A. S. A. C. Diniz, "Distributed photovoltaic generation and energy storage systems: A review," *Renew. Sustain. Energy Rev.*, vol. 14, no. 1, pp. 506–511, Jan. 2010.
[23] A. Pena-Bello, M. Burer, M. K. Patel, and D. Parra, "Optimizing PV and grid charging in combined applications to improve the profitability of residential batteries," *J. Energy Storage*, vol. 13, pp. 58–72, Oct. 2017.
[24] J. Patten, N. Christensen, G. Nola, and S. Srivastava, "Electric vehicle battery — Wind storage system," 2011, pp. 1–3.
[25] K. Clement-Nyns, E. Haesen, and J. Driesen, "The impact of vehicle-to-grid on the distribution grid," *Electr. Power Syst. Res.*, vol. 81, no. 1, pp. 185–192, Jan. 2011.
[26] W. Kempton and J. Tomić, "Vehicle-to-grid power implementation: From stabilizing the grid to supporting large-scale renewable energy," *J. Power Sources*, vol. 144, no. 1, pp. 280–294, Jun. 2005.
[27] T. Sousa, H. Morais, J. Soares, and Z. Vale, "Day-ahead resource scheduling in smart grids considering Vehicle-to-Grid and network constraints," *Appl. Energy*, vol. 96, pp. 183–193, Aug. 2012.
[28] L. Wang, S. Sharkh, and A. Chipperfield, "Optimal coordination of vehicle-to-grid batteries and renewable generators in a distribution system," *Energy*, vol. 113, pp. 1250–1264, Oct. 2016.
[29] B. Tarroja, L. Zhang, V. Wifvat, B. Shaffer, and S. Samuelsen, "Assessing the stationary energy storage equivalency of vehicle-to-grid charging battery electric vehicles," *Energy*, vol. 106, pp. 673–690, Jul. 2016.
[30] M. Marinelli, S. Martinenas, K. Knezović, and P. B. Andersen, "Validating a centralized approach to primary frequency control with series-produced electric vehicles," *J. Energy Storage*, vol. 7, pp. 63–73, Aug. 2016.
[31] J. Neubauer and A. Pesaran, "The ability of battery second use strategies to impact plug-in electric vehicle prices and serve utility energy storage applications," *J. Power Sources*, vol. 196, no. 23, pp. 10351–10358, Dec. 2011.
[32] S. Shokrzadeh and E. Bibeau, "Sustainable integration of intermittent renewable energy and electrified light-duty transportation through repurposing batteries of plug-in electric vehicles," *Energy*, vol. 106, pp. 701–711, Jul. 2016.
[33] C. Heymans, S. B. Walker, S. B. Young, and M. Fowler, "Economic analysis of second use electric vehicle batteries for residential energy storage and load-levelling," *Energy Policy*, vol. 71, pp. 22–30, Aug. 2014.
[34] M. O. Ramoni and H.-C. Zhang, "End-of-life (EOL) issues and options for electric vehicle batteries," *Clean Technol. Environ. Policy*, vol. 15, no. 6, pp. 881–891, Dec. 2013.
[35] Daimler AG, "World's largest 2nd-use battery storage is starting up," *http://media.daimler.com*, Lünen/Stuttgart, 13-Sep-2016.
[36] R. Hein, P. R. Kleindorfer, and S. Spinler, "Valuation of electric vehicle batteries in vehicle-to-grid and battery-to-grid systems," *Technol. Forecast. Soc. Change*, vol. 79, no. 9, pp. 1654–1671, Nov. 2012.
[37] S. Shokrzadeh and E. Bibeau, "Repurposing Batteries of Plug-In Electric Vehicles to Support Renewable Energy Penetration in the Electric Grid," 2012.
[38] THINK Global AS, "THINK City Bedienungsanleitung." 2010.
[39] J. Sudworth, "The sodium/nickel chloride (ZEBRA) battery," *J. Power Sources*, vol. 100, no. 1–2, pp. 149–163, Nov. 2001.
[40] C.-H. Dustmann, "Advances in ZEBRA batteries," *J. Power Sources*, vol. 127, no. 1–2, pp. 85–92, Mar. 2004.
[41] G. Coley, "BeagleBone Black System Reference Manual." The BeagleBoard.org Foundation, 11-Apr-2013.
[42] Logic Supply, "BeagleBone Black Serial Cape Manual." Logic Supply, 20-Feb-2015.
[43] I. Standard, "ISO 11898, 1993," *Road Veh. Digit. Information–Controller Area Netw. CAN High-Speed Commun.*, 1993.
[44] I. Standard, "IEC 61158, 2014," *Ind. Commun. Netw. - Profiles - Part 2 Addit. Fieldbus Profiles Real-Time Netw. Based ISOIEC 8802-3*, 2014.
[45] mes-dea, "Battery Charger E.F." 02-Aug-2007.
[46] Fronius, "Fronius Symo Datasheet." Fronius, 2011.
[47] Algodue, "UEM80." Logic Supply, Mar-2016.

[48] B. Fäßler, P. Kepplinger, M. L. Kolhe, and J. Petrasch, “Decentralized on-site optimization of a battery storage system using one-way communication,” presented at the International Conference on Renewable Power Generation, 2015, p. 1.-7.
[49] EXAA Abwicklungsstelle für Energieprodukte AG, “Spotmarkt,” *EXXA*. [Online]. Available: http://www.exaa.at/de/marktdaten/handelsergebnisse. [Accessed: 18-Dec-2015].
[50] mes-dea, “ZEBRA Battery.” 25-Mar-2008.

APPENDIX

Table 1: ZEBRA battery parameters [50].

Maximum energy content, $E_{\mathrm{el,max}}$	28.2 kWh
Maximum degree of discharge	80%
Open circuit voltage (DC) (100–85% SOC)	371 V
Minimum operation voltage (DC)	248 V
Maximum discharging current (AC)	224 A
Cell type/Number of cells	ML3X/288
Weight with BMS	243 kg
Specific energy	118 Wh/kg
Specific power	168 W/kg
Operating temperature range	-40 to 50 °C
Thermal loss	< 130 W
Minimum discharge time	120 min

Table 2: MES-DEA battery charger parameters [45].

Maximum input current (AC)	15.5 A
Input voltage (AC)	110 – 253 V
Mains frequency	47 – 63 Hz
Operating temperature range	-20 to 40 °C
Output power (DC)	3.2 kW or max 26 A
Weight	7 kg

Table 3: Fronius SYMO 8.2-3-M converter parameters [46].

Maximum input current (DC)	16 A
Input voltage (DC)	200 – 1000 V
Operating temperature range	-25 to 60 °C
Output power (AC)	8.2 kW
Maximum output current (AC)	13.1 A
Weight	21.9 kg

Table 4: Algodue UEM80-4D E parameters [47].

Maximum consumption (each phase)	7.5 VA – 0.5 W

Minimum current (AC)	250 mA
Maximum current (AC)	80 A
Voltage range (AC)	3x230/400 V
Mains frequency	50/60 Hz
Accuracy	Active energy class B according to EN 50470-3 Reactive energy class 2 according to IEC/EN 62053-23
Operating temperature range	-25 to 55 °C